Geochemical Perspectives Letters

© 2026 The Authors
Published by the European Association of Geochemistry

Pyrite records fluid evolution: sulfur sources controls on arsenic speciation and zonation

A.P. Deditius[1], X. Yao[1], F. Xia[1*], J. Brugger[2], Y. Xing[2,3], B.E. Etschmann[2], A. Suvorova[4], M.P. Roberts[4], C.M. Kewish[5]

OPEN ACCESS

https://doi.org/10.7185/geochemlet.2603

Abstract

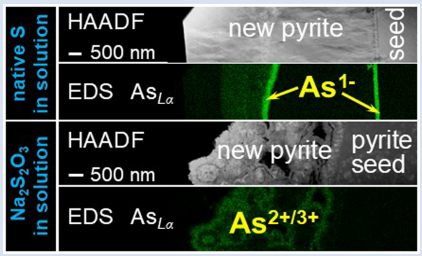

Zoning and speciation of arsenic (As) in pyrite are used to infer changes in the chemical composition of hydrothermal fluids and conditions of ore deposit formation. Yet, the processes controlling the distribution and oxidation state of As during pyrite formation are poorly understood. We report the results of experiments designed to test the capacity of pyrite to record changes in fluid composition under dynamic reaction conditions. When pyrite seeds were exposed alternately to As-bearing and As-free fluids, concentric As-rich (≤6.0 wt. % of As^{1-}) and As-free pyrite overgrowths formed when native S was used as the sulfur source. In contrast, a sodium thiosulfate source produced randomly oriented aggregates of concentrically zoned microparticulate (~1 μm) As-bearing pyrite (<1.5 wt. % of $As^{2+/3+}$), failing to record the changes of fluid composition. We demonstrate that by controlling $H_2S_{(aq)}$ availability, the source of sulfur affects the degree of pyrite supersaturation under conditions relevant to natural hydrothermal systems, which controls the nucleation rate, crystal growth, As uptake, As oxidation state, and consequently, the ability of pyrite to record individual fluid pulses. This sulfur source effect has significant implications for metal incorporation into pyrite and understanding of the formation of many ore deposits.

Received 18 February 2025 | Accepted 16 December 2025 | Published 22 January 2026

Introduction

The incorporation of arsenic and other trace elements into distinct zones during pyrite growth is one of the most prominent features that helps elucidate the evolution of fluid composition during ore deposition (Muntean *et al.*, 2011; Peterson and Mavrogenes, 2014; Morin *et al.*, 2017; Román *et al.*, 2019; Xing *et al.*, 2019). Commonly, pyrite growth zones are arranged in concentric As-rich and As-poor zones (Chouinard *et al.*, 2005) or as spongy porous aggregates of spheroidal particles deposited on barren pyrite (Deditius *et al.*, 2008; Genna and Gaboury, 2015). Lattice bound arsenic in pyrite occurs either as As^{1-} (Simon *et al.*, 1999; Manceau *et al.*, 2020) or $As^{2+/3+}$ (Deditius *et al.*, 2008; Qian *et al.*, 2013; Le Pape *et al.*, 2018), reflecting different incorporation mechanisms. Importantly, the concentrations and oxidation state of As in pyrite are some of the key parameters controlling the incorporation of Au into the mineral and its fate during the formation of gold deposits (*e.g.*, Reich *et al.*, 2005; Deditius *et al.*, 2014; Pokrovski *et al.*, 2021). Changes in the physicochemical parameters of the hydrothermal fluids, such as vigorous *vs.* gentle fluid boiling (Román *et al.*, 2019); the kinetics of crystal growth (Kusebauch *et al.*, 2018; Wu *et al.*, 2019); the type of As source (Qian *et al.*, 2013); and surface chemistry (Fleet and Mumin, 1997) were suggested to account for variable As concentrations, oxidation states, and zoning patterns in pyrite. Yet, the mechanisms controlling As scavenging by pyrite remain poorly understood.

Here, we show that changes in fluid composition affect the formation mechanism of zoned As pyrite overgrowing pyrite seeds (Table S-1). Different S sources, *i.e.* elemental S or thiosulphate ($Na_2S_2O_3{\cdot}5H_2O$), led to contrasting zoning textures and As oxidation states in the overgrowths after hydrothermal treatments that alternated between As-rich and As-free fluids at 200 °C (Table S-2). The aqueous solution compositions involved a mixture of oxidised (HSO_4^-, SO_4^{2-}) and reduced S species (HS^-, $H_2S_{(aq)}$) in the pyrite stability field, relevant for natural hydrothermal systems. Experimental details, analytical methods, and thermodynamic modelling results can be found in the Supplementary Information.

Results

Pyrite morphology, zoning, and composition. Addition of native S resulted in four concentric pyrite growth zones around the seeds (denoted as pyrite-S) (Fig. 1a–e), *i.e.* As-rich (Zones-1, -3) and

1. Sustainable Geochemistry and Mineral Sciences, School of Mathematics, Statistics, Chemistry and Physics, Murdoch University, Perth, WA 6150, Australia
2. School of Earth, Atmosphere and the Environment, Monash University, Clayton, VIC 3800, Australia
3. CSIRO Mineral Resources, Clayton, VIC 3168, Australia
4. Centre for Microscopy, Characterisation and Analysis, The University of Western Australia, Perth, WA 6009, Australia
5. Australian Synchrotron, Clayton, VIC 3168, Australia
* Corresponding author (Email: F.Xia@murdoch.edu.au)

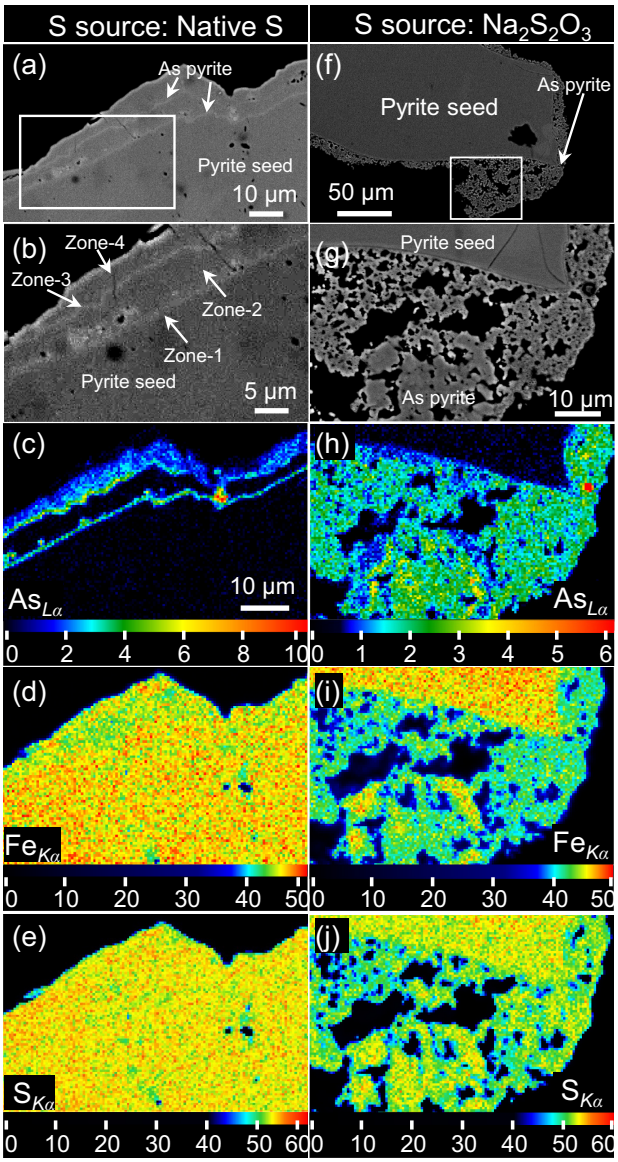

Figure 1 Backscattered electron images **(a, b, f, g)** and elemental mapping of As **(c, h)**, Fe **(d, i)**, and S **(e, j)** in newly formed pyrite. **(a–e)** Pyrite-S, **(f–j)** pyrite-SO. Note four zones of pyrite-S deposited on pyrite seed **(b)** and the sponge-like texture of pyrite-SO.

As depleted or As-free zones (Zones-2, -4). The alternating zones record the imposed variations in fluid composition. However, when native S was replaced with $Na_2S_2O_3{\cdot}5H_2O$, spongy aggregates (5–50 µm) of microparticulate As pyrite (denoted as pyrite-SO) formed instead (Fig. 1f–j); these textures do not reflect the chemical evolution of the system (Fig. 1c,h).

Electron probe microanalysis (EPMA) data show that the As concentrations in Zones-1 and -3 of pyrite-S vary broadly (0.02 to 6.02 wt. %), whereas pyrite-SO contains less As (<1.5 wt. %; Fig. S-1, Table S-3). High angle annular dark field scanning transmission electron microscopy (HAADF-STEM) observations and electron dispersive spectroscopy (EDS) analyses confirm the systematic textural and compositional changes across the four zones in pyrite-S (Figs. 2a,b, S-1 and S-2). Zones-1 and -3 are 200–300 nm thick and contain ≤5.8 wt. % and ≤4.7 wt. % As, respectively; Zones-2 and -4 are 3–5 µm thick and contain As (0.1 and 0.8 wt. %, respectively) near the contact with Zones-1 and -3 (Fig. 2b). Trails of pores occur along the contact between the pyrite seed and Zone-1; between Zones-2 and -3; and within Zone-4 (Fig. 2c–e). High resolution (HR) TEM and electron backscattered diffraction (EBSD) data show that, except for a few spherical misoriented domains (<500 nm) of As-bearing pyrite-S located near the contact between the seed and Zone-1, the lattice orientation of the zoned overgrowth aligns with that of the pyrite seed (Figs. S-3a, b, S-4a). This indicates the predominance of epitaxial growth. The Fast Fourier transformation (FFT) diffraction pattern from the Zone-1 HRTEM image documented rare realgar nanodomains ($d = 3.05$ Å) (Fig. S-5) in quantities below the detection limit of XRD (<0.1 wt. %) (Fig. S-6a).

Pyrite-SO is the only phase detected in the $Na_2S_2O_3{\cdot}5H_2O$ experiments (Fig. S-6b). It comprises concentrically zoned particles, randomly oriented and assembled into aggregates (Figs. 2f,g, S-3c,d, and S-4b). Porosity formed along the contacts between the 50–200 nm thick alternating zones of As-rich and As-poor pyrite (Fig. 2f). Some particles contain oval shaped As-rich (1.1–1.5 wt. %) cores, ~300 nm in diameter, followed by subhedral As depleted zones (0.2–0.7 wt. %), and by a third As enriched zone (~1.4 wt. %) (Fig. 2g). In some particles, a subhedral As depleted core formed first (Figs. S-7, S-8). In pyrite-SO, random As zoning reflects local fluid variations, whereas in pyrite-S the ordered four zone pattern records changes in bulk fluid composition (Figs. 1, 2).

Sulfur source affects arsenic incorporation in pyrite. Pyrite-S compositions plot along the As-S join, indicating the substitution of anionic As^{1-} for S; *i.e.* As substitutes as $[As_2]^{2-}$ for the $[S_2]^{2-}$ dimer (Manceau *et al.*, 2020) (Fig. 3a). In contrast, pyrite-SO compositions form a trend parallel to the Fe-S join towards the As corner of the ternary diagram, indicating cationic $As^{2+/3+}$ substitution for Fe^{2+} (Deditius *et al.*, 2008). These indirect EPMA and EDS results are corroborated by the X-ray absorption near edge structure (XANES) analyses (Fig. 3b,c).

Reaction conditions based on equilibrium thermodynamics. We used activity-activity diagrams to examine As and S speciation in fluids during pyrite formation (Fig. S-9), and aliquot-type thermodynamic modelling to predict reaction paths and mineral compositions resulting from progressive reactions with the two sulfur sources (native S or $Na_2S_2O_3$). These equilibrium models serve as a reference for discussing potential kinetic effects. The sulfur speciation in both systems was buffered near the bisulfide-sulfate boundary, at different bisulfide/sulfate ratios:

$$4S_{(s)} + 4H_2O = 2H^+ + 3H_2S_{(aq)} + SO_4^{2-}\ (3:1\ \text{bisulfide to sulfate}) \quad \text{Eq. 1}$$

$$S_2O_3^{2-} + H_2O = H_2S_{(aq)} + SO_4^{2-}\ (1:1\ \text{bisulfide to sulfate}) \quad \text{Eq. 2}$$

$As(OH)_{3(aq)}$ is the predominant species for As at the pH (~2–6) and redox conditions of the experiments, as it is in most hydrothermal fluids (James-Smith *et al.*, 2010; Testemale *et al.*, 2011). Note that arsenopyrite and realgar are predicted to form in $H_2S_{(aq)}$-rich, reduced ($aH_{2(aq)} > 10^{-10}$) fluids (Fig. S-9a). In our experiments, $H_2S_{(aq)}$ concentrations increase rapidly during sulfur dissolution (Fig. 4a,b), and hence the model predictions are consistent with the presence of small amounts of realgar in pyrite-S (Fig. S-5).

Pyrite is highly supersaturated in the initial solutions with a saturation index (SI) of ~8 for both sulfur sources (Fig. S-10). This SI increases to ~10 in the $Na_2S_2O_3{\cdot}5H_2O$ experiments; but decreases gradually towards ~6 in the S experiments (Fig. S-10). The predicted pH (neutral pH is 5.64 at 200 °C, P_{sat}) is slightly acidic (4.5–5) in the $Na_2S_2O_3{\cdot}5H_2O$ experiments (Fig. 4c), and

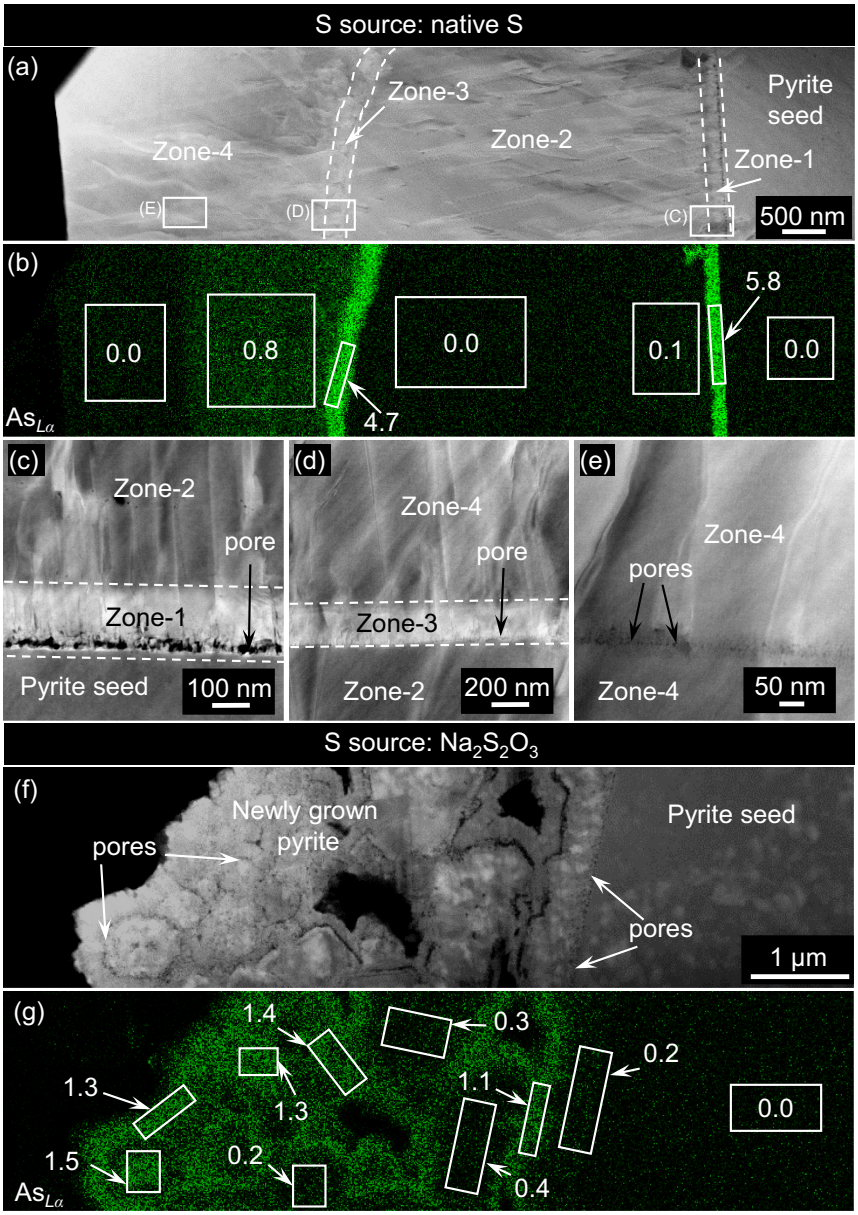

Figure 2 Summary of pyrite textures observed at higher resolution (HAADF-STEM) with corresponding TEM-EDS elemental maps of As. **(a, b)** Alternating As-in (Zones-1, -3) and As-out (Zones-2, -4) zones deposited on pyrite seed. **(b)** The rectangles and the values represent the areas of analysis and the concentration of As (in wt. %). **(c–e)** Porous pyrite formed between the seed and between the zones. **(f, g)** Aggregates of As zoned microcrystalline pyrite-SO. Note the porosity between the pyrite seed and the product and between the As-rich and As-poor zones of pyrite. **(a, b)** Pyrite-S; **(f, g)** pyrite-SO.

rapidly evolves towards more acidic (~3.2) conditions in the S experiments (Fig. 4d). The redox conditions in both experiments remain buffered close to the sulfate-bisulfide equilibrium (Fig. S-9b). The modelling predicts maximum As concentrations of 1000 ppm in pyrite-S and pyrite-SO, lower than the maxima measured in pyrite-S (6.0 wt. %) and pyrite-SO (1.5 wt. %). The predicted As partitioning coefficients between the mineral and fluid decrease by several orders of magnitude in the early stages of the reaction (Fig. 4e,f).

Discussion

Chemical zoning in minerals forms due to changes in fluid composition, temperature, and pressure (Shore and Fowler, 1996), kinetic factors, and/or self organisation (*e.g.*, Rakovan and Reeder, 1996). The alternating As-rich and As-free/poor zones in pyrite-S reflect the pulses of fluids with different compositions, but this record is absent in pyrite-SO (Figs. 1, 2).

The differences between pyrite-S and pyrite-SO are related to the S source, and its effect on the (super-)saturation state of pyrite. First, native S (<1 g/100 mL) is far less soluble than $Na_2S_2O_3{\cdot}5H_2O$ (73 g/100 mL). Second, the progressive disproportionation of thiosulfate (Eq. 2) increases the pyrite supersaturation level, whereas the disproportionation of sulfur (Eq. 1; Liu *et al.*, 2021) is predicted to decrease supersaturation (Fig. S-10). This is mainly because during pyrite precipitation (Fig. S-9), the same amounts of total S added result in a pH increase when using $Na_2S_2O_3{\cdot}5H_2O$, whereas native S causes a rapid pH decrease. This promotes fast nucleation of pyrite-SO and kinetically driven precipitation of spongy aggregates (Figs. 1f–j, 2f,g,

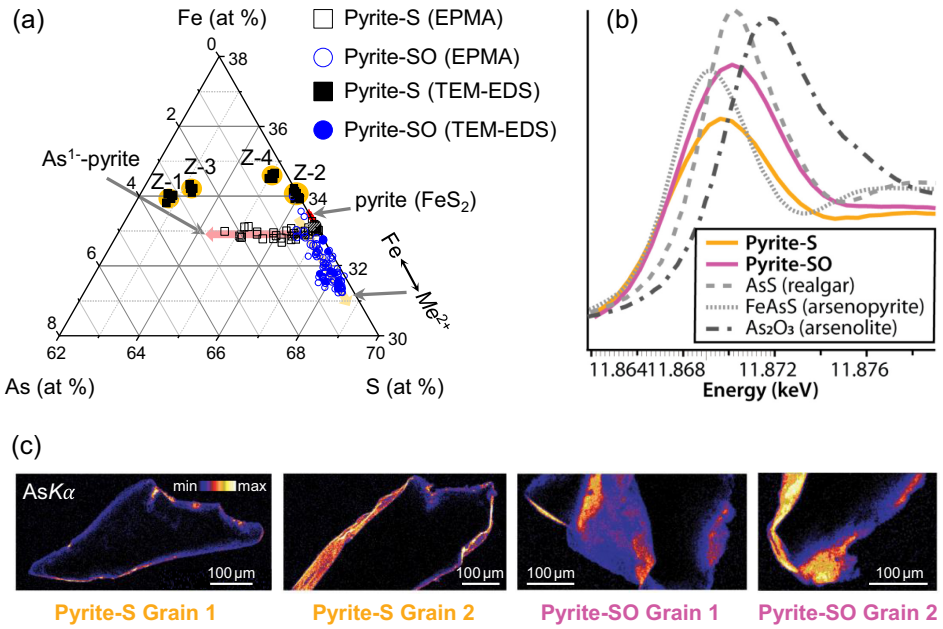

Figure 3 **(a)** Chemical composition of pyrite plotted in the As-Fe-S ternary. Filled symbols indicate the TEM-EDS analyses of Zones-1 to Zone-4 (Z-1 to Z-4). The coloured arrows indicate the trends associated with the substitution of (i) As for S (red), and (ii) Me^{2+} for Fe (yellow). Red cross; starting pyrite. **(b)** XANES spectra obtained on grains in **(c)**. **(c)** XFM maps showing the distribution of As in Pyrite-S (two grains, total 148 kpixel, with ~9000 As-rich) and Pyrite-SO (two grains, total 240 kpixel, including ~20,000 As-rich).

and S-9). In contrast, slower nucleation in the sulfur-bearing experiments resulted in epitaxial growth of pyrite S (Figs. S-3a, S-4a).

The XANES data indicate that As exists predominantly as As^{1-} in pyrite-S (Fig. 3b). Hence, the formation of pyrite-S from dissolved Fe, As and S under acidic conditions is described by:

$$Fe^{2+} + xAs(OH)_{3(aq)} + (2-x)H_2S_{(aq)} = FeS_{2-x}As_{x(s)} + (3x)H_2O + (1-2.5x)H_{2(aq)} + 2H^+ \quad \text{Eq. 3}$$

From the equilibrium constant K_3 of Equation 3, assuming a dilute solution, the value of the molal concentration of $As(OH)_{3(aq)}$ ($[As(OH)_{3(aq)}]$) is equal to the activity (a) of $As(OH)_{3(aq)}$, since $\gamma\ As(OH)_{3(aq)} \approx 1$, where γ is the activity coefficient. Similarly, for a small mole fraction (x) of the $FeAs_2$ component in arsenian pyrite, $\gamma FeAs_2 \approx 1$ according to the standard state based on Henry's law (Supplementary Information); hence, the values of the concentrations of $FeAs_2$ ($[FeAs_2]$, in mole fraction units) are identical to $aFeAs_2$. Using these assumptions, the partitioning coefficient for As between solid and solution is proportional to:

$$\log([FeAs_2]/[As(OH)_{3(aq)}]) \approx 1/x\{2\log K_3 + (5x-2)\log aH_{2(aq)} + 4pH + 2\log aFe^{2+} + x\log a(As(OH)_{3(aq)} + (4-2x)\log aH_2S_{(aq)}\} \quad \text{Eq. 4}$$

This indicates that the As partitioning coefficient is expected to change rapidly during precipitation, depending not only on the amounts of As in solution, but also on pH, redox, and the amounts of dissolved Fe and S. The thermodynamic model of Xing *et al.* (2019) and Equations 3, 4 assume As^{1-} substitution for S in pyrite, requiring a reduction of As^{3+} to As^{1-}. The rapid decrease in the As partitioning coefficient predicted by this thermodynamic model (Fig. 4) is primarily attributed to changes in pH and redox ($a\ H_{2(aq)}$) during the reaction.

In contrast, cationic $As^{2+/3+}$ substitutes for Fe^{2+} in pyrite-SO. Assuming As^{2+}:

$$(1-x)Fe^{2+} + xAs(OH)_{3(aq)} + 2H_2S_{(aq)} = (Fe_{1-x}As_x)S_{2(s)} + (3x)H_2O + (1-x/2)H_{2(aq)} + (2-2x)H^+ \quad \text{Eq. 5}$$

The stability constant K_5 for Equation 5 is:

$$\log([AsS_2]/[As(OH)_{3(aq)}]) \approx 1/x\{\log K_5 + (x/2-1)\log aH_{2(aq)} + (2-2x)pH + (1-x)\log aFe^{2+} + 2\log aH_2S_{(aq)}\} \quad \text{Eq. 6}$$

Compared to anionic As, the incorporation of cationic As is less sensitive to redox.

The thermodynamic modelling shows that the As contents in the pyrite-SO increase with pH when a small amount of S_2O_3 (<~0.15 mole S_{total}) is added (Fig. 4). For pyrite-S, adding similar amounts of native S results in a continuous decrease of As contents in pyrite, coinciding with pH decrease. Overall, the model results indicate that solution chemistry plays a critical role in controlling the precipitation and As content of arsenian pyrite.

Le Pape *et al.* (2017) reported that the polysulfide pathway of pyrite formation generates more oxidising conditions than when reacting FeS with $H_2S_{(aq)}$, facilitating the incorporation of $As^{2+/3+}$. However, incorporation of $As^{2+/3+}$ into pyrite-SO suggests that cationic As in pyrite may not only be related to a relatively higher oxidation state but also to the kinetics of pyrite formation; *i.e.* nucleation is the predominant process for pyrite-SO precipitation at high supersaturation levels, whereas growth is the predominant process for pyrite-S. Thermodynamic modelling suggests that the fluid redox differs only slightly between both experiments ($\Delta\log aH_{2(aq)} < 1$; Fig. 4c,d). The incorporation of $As^{2+/3+}$ introduces structural distortion, which is balanced by the formation of vacancies (Deditius *et al.*, 2008) and is favoured by rapid growth.

Implications for As geochemistry and the formation of ore deposits. The new experiments illustrate how arsenian pyrite

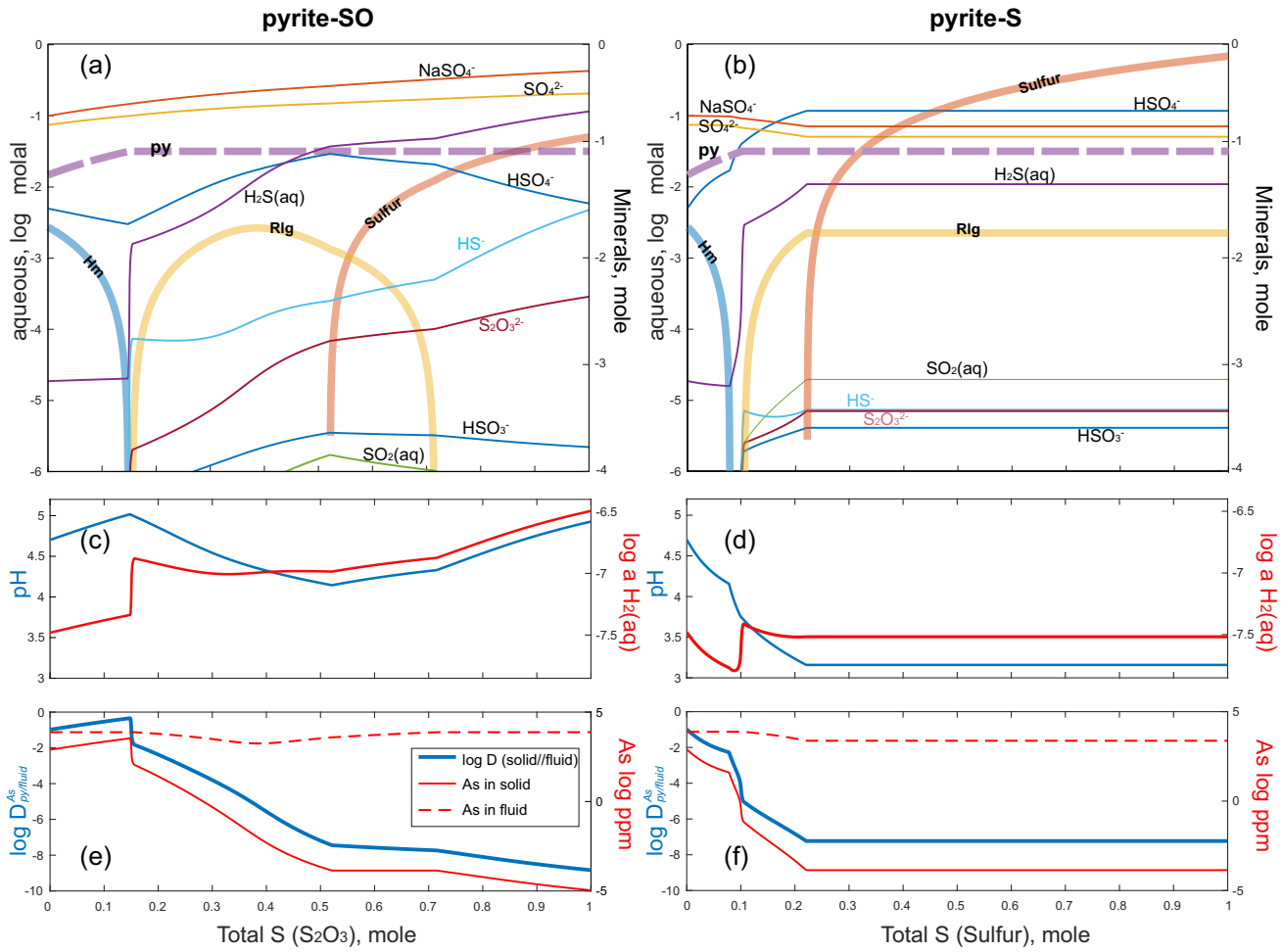

Figure 4 Model results of titrating different S sources as Na sulfite or native sulfur to precipitate arsenian pyrite. **(a, c, e)** The $Na_2S_2O_3$ system, and **(b, d, f)** the native sulfur system. Panels **(a, b)** show the amounts of mineral present (thick lines) and the dominant aqueous sulfur species (thin solid lines). Panels **(c, d)** show redox as *a* $H_{2(aq)}$ (right axes) and solution pH (left axes). Panels **(e, f)** display the variations in As concentrations and partitioning coefficients between pyrite and fluid; $D^{As}_{py/fluid}$ is the partitioning coefficient in ppm and is plotted on the left axis. Mineral abbreviations: py, pyrite; Hm, hematite; Rlg, realgar.

precipitation and associated dynamic changes in fluid composition (pH, redox, As and Fe contents) result in different As speciation (anionic *vs.* cationic As substitution) and variable product morphology arising from different mechanisms of pyrite growth (epitaxial *vs.* nucleation of randomly oriented particles) (Figs. 1–3). Thus, these results help explain the natural variability of pyrite textures in porphyry epithermal, volcanic-hosted massive sulfide (VMS), and Carlin-type ore deposits, as well as in hydrothermal vents. In these dynamic environments, zoned As pyrite forms during fluid boiling/phase separation and/or mixing of seawater or meteoric water with hydrothermal fluids, and/or rapid fluid-rock interactions commonly in the presence of pre-existing pyrite, as documented by changes in S isotopes (Reich *et al.*, 2013; Peterson and Mavrogenes, 2014; Franchini *et al.*, 2015; Román *et al.*, 2019; McLeish *et al.*, 2024; Schaarschmidt *et al.*, 2021; Holley *et al.*, 2024; Xiao *et al.*, 2025). Resulting pyrite textures exhibit a single type, or a mixture of euhedral oscillatory zoned grains (pyrite-S) associated with collomorphic overgrowths and/or aggregates of spongy pyrite (pyrite-SO) reflecting the change in the conditions of the hydrothermal systems.

A higher proportion of oxidised S species is expected during flash vapourisation of hydrothermal fluids at low pressures and/or extreme disproportionation of magmatic SO_2 (Reeves *et al.*, 2011; Peterson and Mavrogenes, 2014). The epitaxial growth of As-bearing pyrite-S resembles the structure of As pyrite in porphyry and epithermal gold deposits (Chouinard *et al.*, 2005; Deditius *et al.*, 2008; Peterson and Mavrogenes, 2014). There, pyrite records the transition from porphyry to epithermal conditions, through As, Au, and chalcophile element-rich rims overgrowing a (Co, Ni)-bearing euhedral porphyry pyrite core (Fig. 1) (Reich *et al.*, 2013; Peterson and Mavrogenes, 2014; Franchini *et al.*, 2015). Porosity aligned with the contact between the As-rich zones and As-free pyrite (Fig. 2) highlights the change in the fluid chemistry. A similar texture was interpreted to signify enrichment of chalcophile elements in arsenian pyrite during fluid boiling in hydrothermal systems (Román *et al.*, 2019). Importantly, the textural changes and porosity (Figs. 1, S-1) from As-rich to As-poor may be the only evidence of changing conditions during continuous growth of pyrite without disturbing the S isotopic signature (McLeish *et al.*, 2024).

The spherical morphology and randomly orientated pyrite-SO, often detached from the pyrite seed (Figs. S-7, S-8), resembles textures in Carlin-type gold deposits formed during mixing of meteoric water and hydrothermal fluids interacting with pre-existing pyrite traps (Muntean *et al.*, 2011; Holley *et al.*, 2024), or those in hydrothermal pyrite precipitated under far from equilibrium conditions of hydrothermal vents during the mixing of the hot fluids with seawater with decreasing $H_2S_{(aq)}$ concentrations (Gartman and Luther, 2013; McLeish *et al.*, 2024; Schaarschmidt *et al.*, 2021). The variable concentrations of As in pyrite-SO

resemble the internally heterogeneous nanoscale concentric As zonation of pyrite from Carlin-type gold deposits, stemming from the partial replacement of pre-existing As-rich zones and liberation of As into the fluid. This process explains the formation of the aggregates of randomly oriented nanoparticles on the sedimentary pyrite or detached from its surface (Holley *et al.*, 2024; Xiao *et al.*, 2025). Epitaxial growth of As pyrite on the pyrite core was explained by means of decoupled dissolution of the core and subsequent precipitation of the As pyrite rim (Xiao *et al.*, 2025).

In nature, most As pyrite contains anionic As substituting for S (Deditius *et al.*, 2014). Epitaxial overgrowth of pyrite by As pyrite (Fig. S-5) or recrystallised As pyrite hosts As^{1-}, while fast nucleation of spherical, randomly oriented pyrite sequesters cationic $As^{2+/3+}$. We find that the incorporation of anionic or cationic As into pyrite (Figs. 1–3) may depend on pyrite saturation levels. At high S concentrations (high supersaturation), pyrite incorporates cationic As, since no (or little) redox reaction is required (Eqs. 3–6; Figs. 1, 2 and 4).

In addition, the ppm-based As partitioning coefficient, $D^{As}_{py/fluid}$ (= [As (ppm) in pyrite/As (ppm) in fluid]) for pyrite-S (~100), is an order of magnitude higher than in pyrite-SO (~12), following the decreasing trend with increasing As concentration in the fluid (Figs. S-11, S-12) (Kusebauch *et al.*, 2018). This may stem from different mechanisms of incorporation of anionic *vs.* cationic As species; thermodynamically controlled (Eq. 2) growth of arsenian pyrite-S and nucleation of pyrite-SO. In nucleation controlled pyrite-SO, the As zoning does not reflect As-rich and As-free pulses, *i.e.* pyrite-SO does not preserve the history of successive fluid inputs (Holley *et al.*, 2024). Consequently, the incorporation of other metals, such as Au, Cu, Co, Ni, and Zn, which often coexist with As (Parnell *et al.*, 2018; Domingos *et al.*, 2023), may be limited, therefore affecting the capability of pyrite to record the composition of the hydrothermal fluid. These results provide important and first hand information on how mineral formation responds to changing fluid chemistry, with implications for a detailed understanding of ore deposit-forming processes.

Acknowledgements

The authors acknowledge funding from the Australian Research Council (DP170101893, DP220100500); the Australian Microscopy and Microanalysis Research Facility at the Centre for Microscopy, Characterisation and Analysis, The University of Western Australia; and The Australian Synchrotron, part of ANSTO, for access to the Powder Diffraction and X-ray Fluorescence Microscopy beamlines. XY acknowledges Murdoch University for a Strategic Scholarship. We are grateful to Gleb Pokrovski, Denis Fougerouse, Duncan McLeish, two anonymous reviewers, and editor Eric Oelkers for their insightful suggestions, which helped us to improve this manuscript.

Editor: Eric Oelkers

Additional Information

Supplementary Information accompanies this letter at https://www.geochemicalperspectivesletters.org/article2603.

© 2026 The Authors. This work is distributed under the Creative Commons Attribution 4.0 License, which permits unrestricted use, distribution, and reproduction in any medium, provided the original author and source are credited. Additional information is available at http://www.geochemicalperspectivesletters.org/copyright-and-permissions.

Cite this letter as: Deditius, A.P., Yao, X., Xia, F., Brugger, J., Xing, Y., Etschmann, B.E., Suvorova, A., Roberts, M.P., Kewish, C.M. (2026) Pyrite records fluid evolution: sulfur sources controls on arsenic speciation and zonation. *Geochem. Persp. Let.* 38, 53–59. https://doi.org/10.7185/geochemlet.2603

References

Chouinard, A., Paquette, J., Williams-Jones, A.E. (2005) Crystallographic controls on trace-element incorporation in auriferous pyrite from the Pascua epithermal high-sulfidation deposit, Chile–Argentina. *The Canadian Mineralogist* 43, 951–963. https://doi.org/10.2113/gscanmin.43.3.951

Deditius, A.P., Utsunomiya, S., Renock, D., Ewing, R.C., Ramana, C.V., Becker, U., Kesler, S.E. (2008) A proposed new type of arsenian pyrite: Composition, nanostructure and geological significance. *Geochimica et Cosmochimica Acta* 72, 2919–2933. https://doi.org/10.1016/j.gca.2008.03.014

Deditius, A.P., Reich, M., Kesler, S.E., Utsunomiya, S., Chryssoulis, S.L., Walshe, J., Ewing, R.C. (2014) The coupled geochemistry of Au and As in pyrite from hydrothermal ore deposits. *Geochimica et Cosmochimica Acta* 140, 644–670. https://doi.org/10.1016/j.gca.2014.05.045

Domingos, J.M., Runge, E., Dreher, C., Chiu, T.-H., Shuster, J., Fischer, S., Kappler, A., Duda, J.-P., Xu, J., Mansor, M. (2023) Inferred pyrite growth via the particle attachment pathway in the presence of trace metals. *Geochemical Perspectives Letters* 26, 14–19. https://doi.org/10.7185/geochemlet.2318

Fleet, M.E., Mumin, A.H. (1997) Gold-bearing arsenian pyrite and marcasite and arsenopyrite from Carlin Trend gold deposits and laboratory synthesis. *American Mineralogist* 82, 182–193. https://doi.org/10.2138/am-1997-1-220

Franchini, M., McFarlane, C., Maydagán, L., Reich, M., Lentz, D.R., Meinert, L., Bouhier, V. (2015) Trace metals in pyrite and marcasite from the Agua Rica porphyry-high sulfidation epithermal deposit, Catamarca, Argentina: Textural features and metal zoning at the porphyry to epithermal transition. *Ore Geology Reviews* 66, 366–387. https://doi.org/10.1016/j.oregeorev.2014.10.022

Gartman, A., Luther III, G.W. (2013) Comparison of pyrite (FeS_2) synthesis mechanisms to reproduce natural FeS_2 nanoparticles found at hydrothermal vents. *Geochimica et Cosmochimica Acta* 120, 447–458. https://doi.org/10.1016/j.gca.2013.06.016

Genna, D., Gaboury, D. (2015) Deciphering the Hydrothermal Evolution of a VMS System by LA-ICP-MS Using Trace Elements in Pyrite: An Example from the Bracemac-McLeod Deposits, Abitibi, Canada, and Implications for Exploration. *Economic Geology* 110, 2087–2108. https://doi.org/10.2113/econgeo.110.8.2087

Holley, E.A., Jilly-Rehak, C., Fulton, A.A., Gorman, B. (2024) Trace Element Zonation in Carlin-Type Pyrite: Tracking Ore-Forming Processes at the Nanoscale. *Economic Geology* 119, 1139–1169. https://doi.org/10.5382/econgeo.5089

James-Smith, J., Cauzid, J., Testemale, D., Liu, W., Hazemann, J.-L., Proux, O., Etschmann, B., Philippot, P., Banks, D., Williams, P., Brugger, J. (2010) Arsenic speciation in fluid inclusions using micro-beam X-ray absorption spectroscopy. *American Mineralogist* 95, 921–932. https://doi.org/10.2138/am.2010.3411

Kusebauch, C., Oelze, M., Gleeson, S.A. (2018) Partitioning of arsenic between hydrothermal fluid and pyrite during experimental siderite replacement. *Chemical Geology* 500, 136–147. https://doi.org/10.1016/j.chemgeo.2018.09.027

Le Pape, P., Blanchard, M., Brest, J., Boulliard, J.-C., Ikogou, M., Stetten, L., Wang, S., Landrot, G., Morin, G. (2017) Arsenic Incorporation in Pyrite at Ambient Temperature at Both Tetrahedral S^{-I} and Octahedral Fe^{II} Sites: Evidence from EXAFS–DFT Analysis. *Environmental Science & Technology* 51, 150–158. https://doi.org/10.1021/acs.est.6b03502

Le Pape, P., Blanchard, M., Juhin, A., Rueff, J.-P., Ducher, M., Morin, G., Cabaret, D. (2018) Local environment of arsenic in sulfide minerals: insights from high-resolution X-ray spectroscopies, and first-principles calculations at the As K-edge. *Journal of Analytical Atomic Spectrometry* 33, 2070–2082. https://doi.org/10.1039/C8JA00272J

Liu, W., Spinks, S.C., Glenn, M., MacRae, C., Pearce, M.A. (2021) How carbonate dissolution facilitates sediment-hosted Zn-Pb mineralization. *Geology* 49, 1363–1368. https://doi.org/10.1130/G49056.1

Manceau, A., Merkulova, M., Mathon, O., Glatzel, P., Murdzek, M., Batanova, V., Simionovici, A., Steinmann, S.N., Paktunc, D. (2020) The Mode of

Incorporation of As(-I) and Se(-I) in Natural Pyrite Revisited. *ACS Earth and Space Chemistry* 4, 379–390. https://doi.org/10.1021/acsearthspacechem.9b00301

McLeish, D.F., Williams-Jones, A.E., Clark, J.R., Stern, R.A. (2024) Extreme shifts in pyrite isotope compositions reveal the path to bonanza gold. *Proceedings of the National Academy of Sciences* 121, e2402116121. https://doi.org/10.1073/pnas.2402116121

Morin, G., Noël, V., Menguy, N., Brest, J., Baptiste, B., Tharaud, M., Ona-Nguema, G., Ikogou, M., Viollier, E., Juillot, F. (2017) Nickel accelerates pyrite nucleation at ambient temperature. *Geochemical Perspectives Letters* 5, 6–11. https://doi.org/10.7185/geochemlet.1738

Muntean, J.L., Cline, J.S., Simon, A.C., Longo, A.A. (2011) Magmatic–hydrothermal origin of Nevada's Carlin-type gold deposits. *Nature Geoscience* 4, 122–127. https://doi.org/10.1038/ngeo1064

Parnel, J., Perez, M., Armstrong, J., Bullock, L., Feldmann, J., Boyce, A.J. (2018) Geochemistry and metallogeny of Neoproterozoic pyrite in oxic and anoxic sediments. *Geochemical Perspectives Letters* 7, 12–16. https://doi.org/10.7185/geochemlet.1812

Peterson, E.C., Mavrogenes, J.A. (2014) Linking high-grade gold mineralization to earthquake-induced fault-valve processes in the Porgera gold deposit, Papua New Guinea. *Geology* 42, 383–386. https://doi.org/10.1130/G35286.1

Pokrovski, G.S., Escoda, C., Blanchard, M., Testemale, D., Hazemann, J.-L., Guoy, S., Kokh, M.A., Boiron, M.-C., de Parseval, F., Aigouy, T., Menjot, L., de Parseval, P., Proux, O., Rovezzi, M., Béziat, D., Salvi, S., Kouzmanov, K., Bartsch, T., Pöttgen, R., Doert, T. (2021) An arsenic-driven pump for invisible gold in hydrothermal systems. *Geochemical Perspectives Letters* 17, 39–44. https://doi.org/10.7185/geochemlet.2112

Qian, G., Brugger, J., Testemale, D., Skinner, W., Pring, A. (2013) Formation of As(II)-pyrite during experimental replacement of magnetite under hydrothermal conditions. *Geochimica et Cosmochimica Acta* 100, 1–10. https://doi.org/10.1016/j.gca.2012.09.034

Rakovan, J., Reader, R.J. (1996) Intracrystalline rare earth element distributions in apatite: Surface structural influences on incorporation during growth. *Geochimica et Cosmochimica Acta* 60, 4435–4445. https://doi.org/10.1016/S0016-7037(96)00244-X

Reeves, E.P., Seewald, J.S., Saccocia, P., Bach, W., Craddock, P.R., Shanks, W.C., Sylva, S.P., Walsh, E., Pichler, T., Rosner, M. (2011) Geochemistry of hydrothermal fluids from the PACMANUS, Northeast Paul and Vienna Woods hydrothermal fields, Manus Basin, Papua New Guinea. *Geochimica et Cosmochimica Acta* 75, 1088–1123. https://doi.org/10.1016/j.gca.2010.11.008

Reich, M., Kesler, S.E., Utsunomiya, S., Palenik, C.S., Chryssoulis, S.L., Ewing, R.C. (2005) Solubility of gold in arsenian pyrite. *Geochimica et Cosmochimica Acta* 69, 2781–2796. https://doi.org/10.1016/j.gca.2005.01.011

Reich, M., Deditius, A., Chryssoulis, S., Li, J.-W., Ma, C.-Q., Parada, M.A., Barra, F., Mittermayr, F. (2013) Pyrite as a record of hydrothermal fluid evolution in a porphyry copper system: A SIMS/EPMA trace element study. *Geochimica et Cosmochimica Acta* 104, 42–62. https://doi.org/10.1016/j.gca.2012.11.006

Román, N., Reich, M., Leisen, M., Morata, D., Barra, F., Deditius, A.P. (2019) Geochemical and micro-textural fingerprints of boiling in pyrite. *Geochimica et Cosmochimica Acta* 246, 60–85. https://doi.org/10.1016/j.gca.2018.11.034

Schaarschmidt, A., Haase, K.M., Klemd, R., Keith, M., Voudouris, P.C., Alfieris, D., Strauss, H., Wiedenbeck, M. (2021) Boiling effects on trace element and sulfur isotope compositions of sulfides in shallow-marine hydrothermal systems: Evidence from Milos Island, Greece. *Chemical Geology* 583, 120457. https://doi.org/10.1016/j.chemgeo.2021.120457

Shore, M., Fowler, A.D. (1996) Oscillatory zoning in minerals; a common phenomenon. *The Canadian Mineralogist* 34, 1111–1126.

Simon, G., Huang, H., Penner-Hahn, J.E., Kesler, S.E., Kao, L.-S. (1999) Oxidation state of gold and arsenic in gold-bearing arsenian pyrite. *American Mineralogist* 84, 1071–1079. https://doi.org/10.2138/am-1999-7-809

Testemale, D., Pokrovski, G.S., Hazemann, J.-L. (2011) Speciation of As^{III} and As^{V} in hydrothermal fluids by *in situ* X-ray absorption spectroscopy. *European Journal of Mineralogy* 23, 379–390. https://doi.org/10.1127/0935-1221/2011/0023-2104

Wu, Y.-F., Fougerouse, D., Evans, K., Reddy, S.M., Saxey, D.W., Guagliardo, P., Li, J.-W. (2019) Gold, arsenic, and copper zoning in pyrite: A record of fluid chemistry and growth kinetics. *Geology* 47, 641–644. https://doi.org/10.1130/G46114.1

Xiao, J., Xie, Z., Xia, Y., Gopon, P., Tan, Q. (2025) Consistent crystal orientation of core and rim pyrites indicates an epitaxial growth of rim in Carlin-type gold deposits. *Geoscience Frontiers* 16, 101966. https://doi.org/10.1016/j.gsf.2024.101966

Xing, Y., Brugger, J., Tomkins, A., Shvarov, Y. (2019) Arsenic evolution as a tool for understanding formation of pyritic gold ores. *Geology* 47, 335–338. https://doi.org/10.1130/G45708.1